

Impact of spatially correlated pore-scale heterogeneity on drying porous media

Oshri Borgman,¹ Paolo Fantinel,² Wieland Lühder,² Lucas Goehring², and Ran Holtzman¹

¹Department of Soil and Water Sciences, The Hebrew University of Jerusalem, Rehovot 7610001, Israel

²Max Planck Institute for Dynamics and Self-Organization (MPIDS), 37077 Göttingen, Germany

Abstract

We study the effect of spatially-correlated heterogeneity on the rate and extent of isothermal drying of porous media. We combine a minimal pore-scale model with microfluidic experiments using a similar pore geometry. Our simulated patterns and rates compare favorably with experiments, considering the large sensitivity of the emergent patterns to the uncertainty introduced by manufacturing errors. We show that increasing the correlation length in particle sizes promotes preferential invasion of large pores, prolonging liquid connectivity and surface wetness and thus higher drying rates for longer periods. Our findings improves our quantitative understanding of how pore-scale heterogeneity impacts drying, which plays a crucial role in a wide range of processes ranging from fuel cells or curing of paints and cements to global budgets of energy, water and solutes in soils.

1 Introduction

Drying of porous media plays a crucial role in many natural and industrial systems, from soils, to curing of cement, paints and food [Prat, 2011; Goehring *et al.*, 2015]. Drying in soils is of particular importance for the environment, as it controls the transfer of water as well as energy between the subsurface and the atmosphere and affects solute distribution in the root zone [Or *et al.*, 2013]. The rate and extent of fluid transport in general, and drying in particular, intimately depend on the heterogenous distribution of grain and pore sizes and their connectivity, among other factors [Bultreys *et al.*, 2016; Holtzman, 2016]. Pore-size heterogeneity, random (disordered) as well as correlated, in the form of patches or layers of finer or coarser particles is abundant and an inherent property of natural porous media such as soils or sediments [Knackstedt *et al.*, 2001], for instance as a result of deposition and diagenetic processes. Even in engineered systems such as micromodels, heterogeneity is inevitable due to manufacturing errors.

In this paper, we investigate how spatial correlation in particle sizes affects isothermal drying, where evaporation is driven by vapor concentration differences between the medium and the dryer atmosphere. Evaporation reduces the liquid pressure, allowing air to invade once the capillary entry thresholds are exceeded, forming an interface (also termed drying or evaporation front) separating liquid- and air-filled pores [Lehmann *et al.*, 2008; Shokri *et al.*, 2010]. The drying process is typically divided into two main stages. During stage 1 (also denoted “constant rate period”), evaporation occurs mostly from wet patches at the medium’s surface, which remain wet as long as liquid is supplied by continuous pathways from the medium’s interior. Stage 1 is characterized by a relatively high and constant drying rate, due to an air boundary layer that develops outside the medium [Lehmann *et al.*, 2008; Shokri *et al.*, 2010; Shahraeeni *et al.*, 2012; Goehring *et al.*, 2015]. Stage 2 (or “falling-rate period”) is marked by disruption of liquid pathways to the surface, forcing them to dry out and the evaporation front to recede further away from the surface; consequently, the rate, which becomes limited by vapor diffusion within the porous medium, drop continuously [Lehmann *et al.*, 2008; Shokri *et al.*, 2010; Goehring *et al.*, 2015].

Previous studies have shown that when a sharp contrast in pore sizes exists (in the form of a coarser and finer region, i.e. bimodal size distribution), the coarser region dries up completely before finer pores starts to dry. This has been demonstrated experimentally for a variety of media of different length scales, including sands [Lehmann and Or, 2009; Nachshon *et al.*, 2011], micromodels [Pillai *et al.*, 2009] and colloidal drops [Xu *et al.*, 2008]. Theoretically it has been shown that increasing the width of the pore-size distribution prolongs stage 1 by maintaining liquid connectivity for longer periods [Metzger and Tsotsas, 2005; Lehmann *et al.*, 2008]. Even for the more general problem of immiscible fluid-fluid displacement, there are relatively few studies addressing the impact of spatial correlation. For instance, it has been shown that increasing correlation length decreases the residual saturation of the wetting phase at breakthrough [Ioannidis *et al.*, 1993; Knackstedt *et al.*, 2001], leads to a more gradually-varying capillary pressure-saturation relation [Rajaram *et al.*, 1997; Mani and Mohanty, 1999], and improves connectivity and hence relative permeability of both phases [Mani and Mohanty, 1999]. In conclusion, quantitative understanding of how correlation length affects drying is lacking.

Here, we present a systematic investigation of the impact of spatial correlations in particle size on the drying rate and patterns in porous media. We use pore network modeling complemented with microfluidic experiments to obtain a rigorous quantitative analysis and understand the underlying mechanisms. We show that increasing the correlation length promotes preferential invasion, hence preserving liquid connectivity and surface wetness, delaying the transition between the drying stages.

2 Methods

One of the main challenges in studying fluid displacement processes including drying is their large sensitivity to pore-scale details [Bultreys *et al.*, 2016]. This sensitivity requires multiple realizations for each set of conditions to obtain a statistically-representative description [Mani and Mohanty, 1999]. Here, we formulate a simple model used in computer simulations to generate a sufficiently-large data set to overcome this sensitivity, and validate it using microfluidics providing unprecedented manufacturing and measurements resolution.

As we are interested in fundamental understanding of the underlying mechanisms rather than an accurate quantitative description of specific materials, we choose a simplified analog of disordered porous medium as our model system: cylindrical solid pillars (“particles”) placed on a regular square lattice, where heterogeneity is achieved by varying particle sizes. We consider a horizontal sample to avoid gravity effects, open to the atmosphere at one of its sides where vapor is allowed to diffuse outside and air can invade inside the medium (Fig. 1). We formulate a “minimal” model in the sense that it describes the essential pore-scale physics—including evaporation from interfaces, vapor diffusion, and capillary invasion, via a set of simple rules for interactions between pores. Our numerical model is described below, together with a brief description of our microfluidic experiments. Further details of our experiments and discussion on how such a minimal model captures the observed experimental behavior appears in Fantinel *et al.* [2016].

2.1 Pore Network Model

We develop a pore-network model to simulate isothermal drying of a liquid-filled porous media, discretizing the pore space into pores (the space between four neighboring pillars) interconnected by throats (constriction between two adjacent pillars; Fig. 1). Our model also includes the air boundary layer that develops above the medium’s open surface [Shahraeeni *et al.*, 2012].

The rate of evaporation of liquid from gas-liquid interfaces is computed assuming it is set by the rate of vapor diffusion away from the interface. This assumption allows us to treat evaporation sites as source terms for vapor, and compute vapor concentrations in the entire

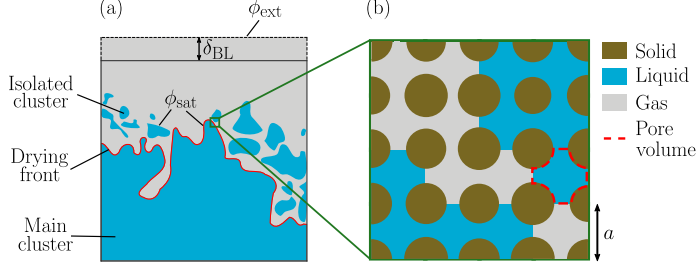


Figure 1. Schematics of our model of a porous media undergoing isothermal drying. A sample is open to the atmosphere at one of its faces (a). Low vapor concentration at the boundary layer’s edge, $\phi = \phi_{\text{ext}}$, drives evaporation and vapor diffusion from air-liquid interfaces (drying front, where $\phi = \phi_{\text{sat}}$). Evaporation reduces liquid pressure, causing air to invade into liquid-filled pores. Some of the liquid disconnects from the bulk (“main cluster”) and becomes isolated. The atmospheric demand of vapor is modeled through a diffusive boundary layer of thickness δ_{BL} . We model evaporation, vapor diffusion and capillary invasion via a pore network model (b). Pores are defined as the space between solid particles (of radius R) placed on a square lattice (spacing a), and are interconnected by throats (aperture w).

domain—air-filled pores as well as the boundary layer—by resolving the mass balance of vapor. A further simplification is provided by the much shorter timescale of vapor diffusion relative to that of liquid transport and interface advancement, allowing us to represent the evolution of the drying front as a sequence of steady state configurations. With this, vapor concentrations are obtained by enforcing the continuity equation in each pore (or boundary layer cell) i ,

$$\sum_j J_{ij} A_{ij} = 0 \quad (1)$$

where the summation is done over neighboring pores (or cells) j , and

$$J_{ij} = -\rho_v^{\text{sat}} D_{\text{eff}} \nabla \phi|_{ij} \quad (2)$$

is the vapor mass flux between two adjacent pores i and j , driven by the local gradient of vapor concentration (in terms of relative humidity, $\phi \in [0, 1]$), $\nabla \phi|_{ij} = (\phi_j - \phi_i)/l_{ij}$. Throat ij connecting pores i and j has a cross-sectional area of $A_{ij} = h w_{ij}$, where w_{ij} is its aperture ($w_{ij} = a$ for boundary layer cells) and h is the pillar height (out of plane sample thickness). Here, ρ_v^{sat} is the saturated vapor density.

The distance l_{ij} is taken to be the lattice spacing a if both pores are gas-filled, and in boundary layer cells. For a gas-filled pore i along the drying front, we set $\phi_j = \phi_{\text{sat}} = 1$ as a boundary condition for the diffusion problem, where J represents the local evaporation rate, with $l_{ij} = a/2$. Other boundary conditions are fixed concentration, $\phi = \phi_{\text{ext}} = 0$, at the edge of the diffusive boundary layer, and no-flow at all faces not open to the atmosphere. This provides a set of linear equations, which we solve explicitly for ϕ in each pore. The effective porous medium diffusion coefficient is $D_{\text{eff}} = \alpha D$, where D is the binary diffusion coefficient in air, with $\alpha = 1.6$ for the porous mediums (determined by finite-element simulations at the sub-pore scale) and $\alpha = 1$ for the boundary layer.

Invasion of air into liquid-filled pores depends on the local capillary pressure, or equivalently, the meniscus curvature (where the two are related via the Young-Laplace law). We relate the change in curvature to changes in liquid volume by approximating each throat as a capillary tube with similar dimensions, $h \times w_{ij}$. We further simplify computations by considering a spherical meniscus in a cylindrical tube with an effective radius of $r_{ij} = (1/h + 1/w_{ij})^{-1}$, such that $C_{ij}^* = 2/r_{ij}$ is the critical curvature for throat ij (invasion occurs when $C \geq C_{ij}^*$). With the above, the curvature of a meniscus C can be updated according to the liquid volume

evaporated from it, ΔV_{ij} , by

$$\Delta V_{ij} = \frac{\pi(2/C)^3}{3} \left(1 - \sqrt{1 - \left(\frac{C}{C_{ij}^*} \right)^2} \right)^2 \left(2 + \sqrt{1 - \left(\frac{C}{C_{ij}^*} \right)^2} \right). \quad (3)$$

To resolve the curvatures of all menisci from the evaporated volume, we use the following closure relations: (1) the total liquid volume decrement from the entire cluster equals the sum of volumes ΔV_{ij} decreased from all menisci ij in that cluster; and (2) the curvature of all menisci in a cluster remains uniform (equal to C). The latter is justified by the much faster pressure diffusion in liquid than of vapor diffusion in air, allowing us to consider instantaneous liquid pressure equilibration. The liquid volume evaporated from each throat during a time step Δt is $\Delta V_{ij} = \Delta t J_{ij} A_{ij} / \rho_l$, where ρ_l is the liquid density.

Once a pore is invaded, the liquid volume associated with it is redistributed to other interfacial pores in that cluster, decreasing the cluster's curvature C according to Eq. 3. Since C is uniform, every meniscus receives a different volume. We restrict the amount of liquid that can be redistributed by enforcing $C \geq 0$; in cases where the redistributed volume is smaller than that associated with an invaded pore, that pore will be considered dry only when all its excess liquid (which could not be redistributed) will evaporate.

2.2 Generating Correlated Geometries

To generate samples with a prescribed spatial correlation in particle sizes ζ , we first generate surfaces with correlated topography (where height represents pillar size), by summing 1000 sine waves with random phases and wave numbers selected from a Gaussian distribution. The width of this distribution in Fourier space is inversely proportional to ζ . We then transform the normally-distributed values into a uniform distribution and rescale to obtain the desired range of pillar sizes, $\bar{R}[1 - \lambda, 1 + \lambda]$, where \bar{R} is the mean pillar radius (overbar denotes arithmetic average) and λ is the imposed disorder.

The parameter values used in this paper are: $a = 130 \mu\text{m}$, $\bar{R} = 50 \mu\text{m}$, $\bar{w} = 30 \mu\text{m}$, $h = 40 \mu\text{m}$, and $\lambda = 0.1$, with a mean porosity of 0.53. Sample size is 100×100 pillars. For each ζ value we generated a set of 40 realizations (varying the random seed while keeping similar statistics, i.e. similar λ and ζ), for ζ of 0, 1, 1.5, 2, 2.5, 3, 4, 6, 10, and 15. Due to the formation of sample-spanning patches for $\zeta = 15$, potentially introducing sample-scale effects, we do not include these simulations in the quantitative analysis along with other ζ values. For completeness, comparison of experimental and simulated patterns for $\zeta = 15$ is presented in Supporting Information.

2.3 Microfluidic Experiments

Micromodels made of an array of cylindrical pillars in between two planar plates are manufactured using standard microfluidic techniques including soft lithography, as briefly described below; for further details see *Fantinel et al.* [2016]. Here the pillar array is ordered on a square lattice; however our procedure allows manufacturing of other designs such as a triangular lattice or a random close packing. A silicon wafer is spin-coated with a negative photoresist (SU8 3025, MicroChem Corp.), which is then exposed to UV light through a mask to produce the desired design (pillar positions and sizes). After rinsing, the remaining SU8 structure is used as a primer for a secondary mold of polydimethylsiloxane (PDMS). The PDMS is then cured and is used as a mold for the final model, made of Norland Optical Adhesive 81 (NOA, Sigma-Aldrich). The NOA sample is then cured and exposed to white light to stabilize its optical properties as well as wettability. Finally, the sample is cut open at one of its sides.

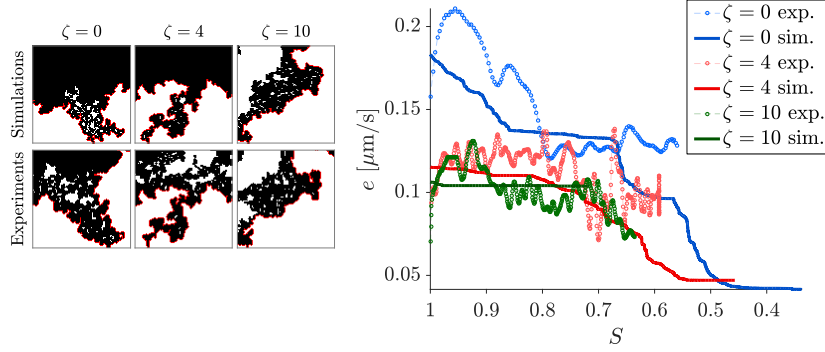


Figure 2. (a) Simulated and experimental patterns for three samples with different correlation length ζ are generally in good agreement, except for the near-surface isolated clusters that persist longer in the experiments. Black and white denote pores filled with air and liquid, respectively, and the red line indicates the drying front. (b) Simulated rates mostly follow the experimental ones, however exhibit a faster rate drop at lower saturation, associated with the faster disappearance of isolated clusters that dry out and force the evaporation front deeper into the medium.

Our manufacturing procedure resolution is $2 \mu\text{m}$. We estimate the uncertainty in pillar sizes to be $\sim 1.6 \mu\text{m}$ ($\sim 3.2\%$ of design). Experiments were conducted on samples with $\zeta = \{1, 4, 10, 15\}$ with $\lambda = \{0.1, 0.2\}$, and $\zeta = 0$ with $\lambda = \{0.03, 0.05, 0.1, 0.2\}$. The NOA samples are first filled with a volatile fluorinated oil (Novec 7500 Engineered Fluid). Then, they are placed in a temperature and humidity controlled environment to evaporate while taking time-lapse images. Images are analyzed to produce discrete, pore-by-pore invasion data and to compute the drying rates. Experiments are stopped at breakthrough.

3 Results

3.1 Comparing Model with Experiments

3.1.1 Drying Patterns

Our simulated drying patterns agree well with patterns in microfluidic experiments using identical pore geometries (Fig. 2a; additional patterns are provided as Supporting Information), with an average match of 59% (standard deviation of 19%). For a given pair of simulated and experimental patterns, the match is the number of *overlapping* invaded pores (in both patterns) divided by the average number of invaded pores, at breakthrough. Other metrics including the front roughness and the main cluster saturation also show good agreement; an exception is the Euler number—the invading phase connectivity computed as the number of clusters of air-filled pores minus the number of liquid pores (“holes”) within them—which does not [Fantinel *et al.*, 2016]. This disparity is due to isolated liquid clusters that form and persist in the experiments, whereas in the simulations fewer clusters form and dry out faster. Consequently, when considering the leading front only (by ignoring small isolated clusters, as often done to estimate finger width [Toussaint *et al.*, 2012]), the pattern agreement improves (average of 64% with a standard deviation of 22%).

3.1.2 Drying Rates

Our simulated drying rates are also in good agreement with experiments, with the exception of low saturations where the faster disappearance of isolated clusters near the surface forces the evaporation front to recede deeper into the medium, and the simulated rate to drop

(Fig. 2b). Note the noise in experimental rates, introduced by image analysis of the time-lapse images [Fantinel *et al.*, 2016]. To examine the impact of the drying pattern on rate, we computed the rates (using Eqs. 1–2) corresponding to the pore-by-pore sequence of experimental configurations; these computed rates match well the experimental ones, suggesting that the mismatch in rates is associated with the disparity in patterns. This agreement also confirms the validity of our model’s evaporation and vapor transport calculation.

3.2 Impact of Spatial Correlation

3.2.1 Drying Patterns

Our simulations demonstrate that increasing the correlation length ζ promotes preferential drying and earlier breakthrough (Fig. 3a). As ζ increases, enhanced connectivity of pores of similar size leads to invasion of larger pores, while smaller pores maintain liquid connectivity to the surface. The preferred drying of large pores leads to a pattern which follows more closely the underlying pore geometry (Fig. 3a). Similarly, the tendency to invade larger pores, quantified here by χ_L , the fraction of larger than average invaded pores (normalized by the total number of invaded pores), increases with ζ (Fig. 3b). Another consequence of preferential drying is that it reaches deeper parts of the medium. This is demonstrated by the increase in drying front depth, \overline{Z}_0 (the center of mass of the invaded pores), with ζ (Fig. 3c). All data in the remainder of the paper (Figs. 3–7), unless noted otherwise, is obtained from sets of 40 realizations, one set for each ζ , showing ensemble mean and standard error.

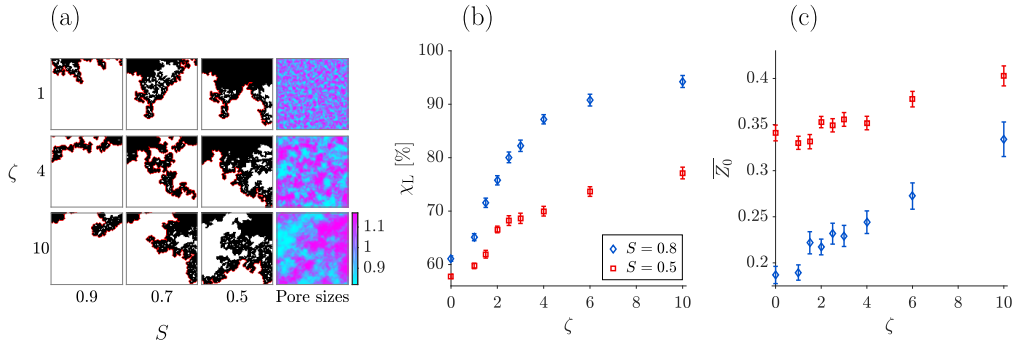


Figure 3. Simulations showing that increasing correlation length ζ promotes preferential drying of connected large pores while avoiding smaller pores, such that the drying pattern follows more closely the underlying sample geometry (a). Patterns at three different saturations, $S = 0.9, 0.7$ and 0.5 , are shown in the leftmost columns. Rightmost column shows the pore size distribution (normalized by the mean). The tendency for preferential drying is quantified by the fraction of large invaded pores, χ_L (b), and the mean invasion depth, \overline{Z}_0 (c). Mean values are calculated from 40 realizations for each ζ value, error bars represent standard error.

3.2.2 Drying Rates

As a consequence of preferential drying of large connected pores, connectivity of wet smaller pores to the medium’s interior is maintained. This preserves surface wetness, prolonging stage 1 and delaying liquid disconnection and resulting rate drop that mark the onset of stage 2 [Lehmann *et al.*, 2008; Shokri *et al.*, 2010; Shahraeeni *et al.*, 2012]. Accordingly, we observe a faster saturation S drop with time t , and maintenance of higher rates \tilde{e} for longer duration (in terms of S), in samples with longer correlations ζ (Fig. 4a–b). The effect of ζ on rate is quantified here through the increasing rate at $S = 50\%$, \tilde{e}_{50} , and the decreasing time until $S = 50\%$ is reached, t_{50} , as ζ is increased (Fig. 4c–d). Here, we use the following

non-dimensional rate and time: $\tilde{e} = e/e_0$ where $e_0 = (\rho_v^{\text{sat}}/\rho_l)D\phi_{\text{sat}}/\delta_{\text{BL}}$ is the potential drying rate, and $\tilde{t} = t/t_0$ where $t_0 = nL/e_0$ is the characteristic time to evaporate liquid from a sample of depth L and porosity n .

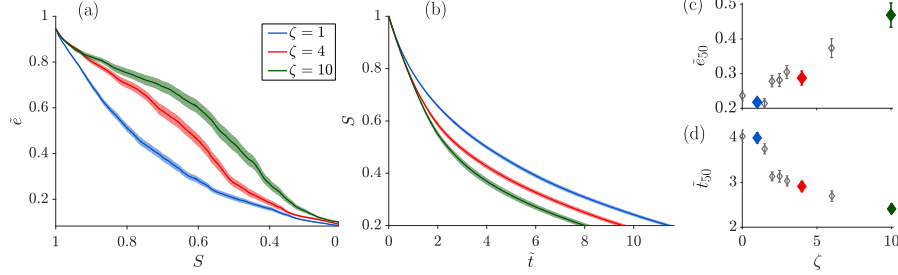


Figure 4. Increasing correlation length ζ maintains liquid connectivity to the surface and hence faster drying rates \tilde{e} for longer duration (a), such that the saturation S drops faster with time \tilde{t} (b). Quantitatively, increasing ζ increases the rate at $S = 50\%$, \tilde{e}_{50} (c), and decreases the time to reach $S = 50\%$, \tilde{t}_{50} (d). See text for definitions of dimensionless rate and time. The values plotted for each ζ are ensemble average (lines in a–b, diamonds in c–d) and standard error (shading in a–b, error bars in c–d) from 40 realizations

4 Discussion

4.1 Predictive model capabilities: Simulations vs. experiments

Our simulated patterns and rates are generally in good agreement with microfluidic experiments using similar pore geometry. This is demonstrated quantitatively by the pattern match (Section 3.1), front roughness and main cluster saturation [Fantinel *et al.*, 2016]. The main difference is the reduced formation and persistence of isolated clusters (quantified by the Euler number [Fantinel *et al.*, 2016]) in the simulations, leading to a faster rate drop than observed experimentally. This difference could be attributed to wettability effects [Shokri *et al.*, 2009]. A highly-wetting fluid such as the oil used here (contact angle of $\sim 3^\circ$) tends to break and form rings around contact lines between the pillars and the substrate. Even if these rings do not significantly affect liquid transport directly, their evaporation would locally affect vapor diffusion. To examine the potential impact of wettability we compare an experiment with oil to one with a less-wetting liquid, water (contact angle of $\sim 70^\circ$). The two experiments mainly differ by the number of isolated clusters, suggesting that wettability effects, which are not included in our model, are a potential source for the disparity in patterns [Fantinel *et al.*, 2016].

An inevitable source of disagreement in patterns—and consequently in rates—even when ignoring isolated clusters, is manufacturing errors introducing uncertainty in pore geometry. Even with our state-of-the-art manufacturing procedure, small random errors ($\sim 1.6 \mu\text{m}$, $\sim 3.2\%$ of the design) in pillar radius occur. We stress that the emergent patterns (in drying, and, in general, immiscible displacement) are highly sensitive to small geometrical details; that is, slight changes in pore sizes, even locally, can significantly alter the pattern. An extreme example of this sensitivity is the “binary choice” that can occur when the invasion front reaches a bottleneck in the form of a narrow throat; if slightly altered, the invasion may proceed elsewhere bypassing an entire region. Such a case is presented in Supporting Information (Fig. S3, $\lambda = 0.2$, $\zeta = 15$), showing distinctively different patterns from two different samples made from the same mold (identical design).

To quantify the sensitivity of the drying pattern to perturbations in pore geometry, we introduce numerically random noise in pillar sizes to a given sample design. Simulations with

different noise values (10 realizations for each) shows that the pattern match drops to $\sim 70\%$ when the error reaches 1.5% (Fig. 5a). The fact that we obtain a comparable match between simulations and experiments indicates that our model predicts patterns very well within the experimental uncertainty in pillar sizes ($\sim 3.2\%$, cf. Fig. 5a). To further emphasize this point, we show that the match between two patterns from a given sample design perturbed by 3% is similar to that between that sample and another realization (different random seed) with pillar sizes difference of 7% (Fig. 5b–d).

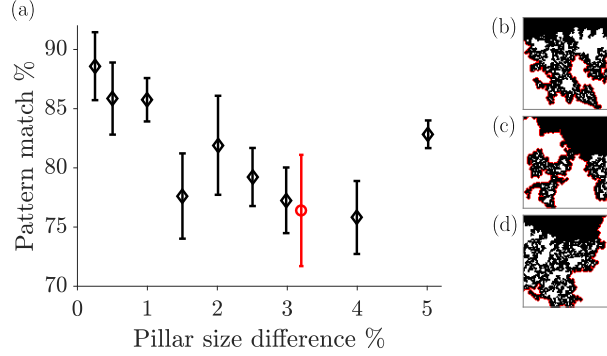


Figure 5. Introducing random noise in pillar sizes leads to significant differences in invasion patterns, with $\sim 77\%$ when the error introduced reaches 1.5%, demonstrating the sensitivity of the emergent pattern to small details (a). Within the experimental uncertainty in pillar sizes ($\sim 3.2\%$, in red), our simulated patterns agrees very well with the experimental ones. As an example, we show that the difference in patterns associated with random error of 3% (b vs. c, match of 72%) is similar to that obtained by comparing with a different realization, where the difference in pillar size is 7% (c vs. d, match of 78%). Pattern match here is computed for the leading front (excluding isolated clusters) at $S = 50\%$.

4.2 Impact of Correlation Length on the Underlying Mechanisms

The increasing tendency to preferentially invade large pores as the correlation length increases can be characterized via the evolution of the liquid pressure. Each time the invasion front reaches a narrow constriction, a substantial liquid pressure drop (via evaporation) is required to overcome the large capillary threshold. In a medium with non-correlated heterogeneity, the frequency of such events is high; in contrast, if pores of similar sizes are interconnected, drying pattern can breakthrough with a low frequency of such events. Indeed, in samples with higher ζ we observe a more gradual change in critical (minimum) pressure p_{inv} with saturation (Fig. 6a), in accordance with observations from drainage simulations [Rajaram *et al.*, 1997]. Here p_{inv} is the minimum liquid pressure (inset of Fig. 6a), normalized by a characteristic invasion pressure $p^* = 2\sigma(\bar{w}^{-1} + h^{-1})$, where σ is the air-liquid interfacial tension. The preferential drying of larger pores maintains surface wetness (of smaller pores) for longer durations (Fig. 6b). Due to the strong influence of surface wetness on the evaporation rate [Shahraeeni *et al.*, 2012], this results in faster drying (Fig. 4).

The maintenance of surface wetness significantly impacts the transition the different drying stages, that is between dominance of evaporation from the open surface, and from deeper parts of the medium’s interior [Lehmann *et al.*, 2008]. Our pore-scale data allows us to quantify the relative strength of these mechanisms. We show that increasing spatial correlation delays this transition (Fig. 7), defined here as the saturation at which evaporation rate from the surface equals that from interior pores, S_{eq} (Fig. 7, inset). This finding has important consequences, as the two mechanisms depend on different properties—surface porosity and transport properties of the medium’s interior at stage 1 and 2, respectively. For instance,

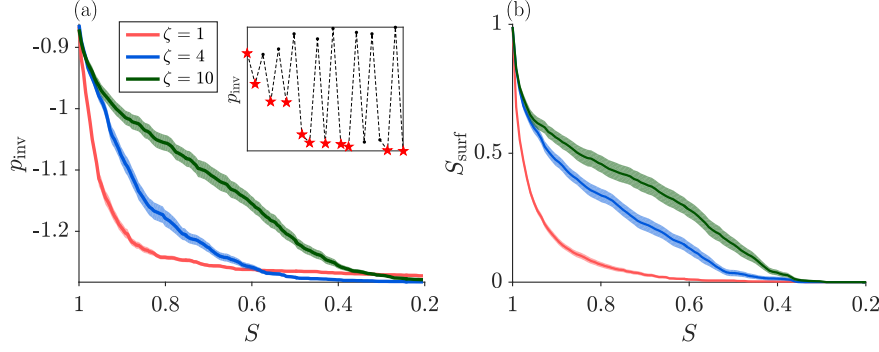


Figure 6. The preferential drying of larger pores in correlated media ζ leads to a more gradual change in the invasion pressure, p_{inv} . Here p_{inv} is obtained from the minimum liquid pressure (a, inset; minimums marked with red stars). Another consequence of preferential drying is the maintenance of surface wetness, S_{surf} , at higher saturations (b), which, due to the strong influence of surface wetness on evaporation rates (b, inset), results in faster drying. Lines and shading represent ensemble average and standard error from 40 realizations.

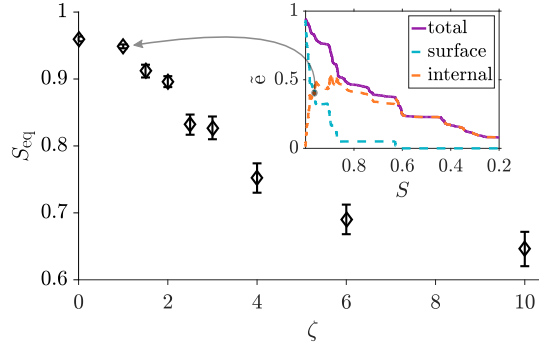


Figure 7. The transition between the drying stages is delayed as the correlation length ζ increases. The transition is defined as the saturation at which evaporation rate from surface pores equals that from internal pores, S_{eq} (inset). Diamonds and error bars show ensemble average and standard error from 40 realizations.

manipulation of the surface microstructure [Lehmann and Or, 2013] could be used to control the duration of faster rate during stage 1.

5 Conclusions

We study the impact of spatially correlated pore geometry on isothermal drying of porous media. We present a minimal pore-scale model, describing evaporation, vapor diffusion, and capillary invasion by a set of simple rules for interactions between pores. We compare our numerical simulations to state-of-the-art microfluidic experiments using a similar pore geometry. Our simulated patterns and rates compare favorably with experiments, considering the large sensitivity of the emergent patterns to the uncertainty in pore geometry introduced by manufacturing errors. We note the reduced formation and persistence of isolated clusters in simulations, leading to a faster rate drop than observed experimentally, which could be explained by wettability effects which are not included in our model.

We find that increasing the correlation length in particle sizes promotes preferential invasion of connected large pores, which preserves liquid connectivity and surface wetness, maintaining higher drying rates for longer periods. We explain this behavior by quantifying the point of transition between dominant mechanisms: from evaporation mostly at the surface where the rate is mainly controlled by diffusion through the boundary layer, to evaporation from depth at a rate limited by the much slower vapor diffusion in the porous medium.

Our approach of coupling pore-scale simulations using a minimal model with high-resolution microfluidic experiments as a simple 2-D analog for porous and granular media, could be applied to study how pore-scale heterogeneity affects a wide range of problems including immiscible fluid-fluid displacement [Holtzman, 2016] or solute transport [Kang *et al.*, 2015]. Specifically, our findings improve our understanding of how pore-scale heterogeneity, inevitable in most porous materials, affects their drying rate and extent. These findings bear significant implications for multiple industrial and natural processes, ranging from fuel cells [Prat, 2011], cements and paints [Goehring *et al.*, 2015] to soil-atmosphere energy and moisture exchange and soil salinization [Nachshon *et al.*, 2011; Norouzi Rad *et al.*, 2013; Or *et al.*, 2013].

Acknowledgments

Financial support by the Niedersachsen-Israel Research Cooperation Program (#xxx) is gratefully acknowledged. RH also acknowledges partial support from the Israeli Science Foundation (#ISF-867/13) and the Israel Ministry of Agriculture and Rural Development (#821-0137-13).

References

- Bultreys, T., W. De Boever, and V. Cnudde (2016), Imaging and image-based fluid transport modeling at the pore scale in geological materials: A practical introduction to the current state-of-the-art, *Earth-Science Rev.*, 155, 93–128, doi:10.1016/j.earscirev.2016.02.001.
- Fantinel, P., O. Borgman, R. Holtzman, and L. Goehring (2016), Validating pore-scale models through microfluidic experiments.
- Goehring, L., A. Nakahara, T. Dutta, S. Kitsunezaki, and S. Tarafdar (2015), *Desiccation Cracks and their Patterns: Formation and Modelling in Science and Nature*, vol. 53, 368 pp., doi:10.1002/9783527671922.
- Holtzman, R. (2016), Effects of Pore-Scale Disorder on Fluid Displacement in Partially-Wettable Porous Media, *Scientific Reports*, 6, 36,221, doi:10.1038/srep36221.
- Ioannidis, M. A., I. Chatzis, and E. A. Sudicky (1993), The effect of spatial correlations on the accessibility characteristics of three-dimensional cubic networks as related to drainage displacements in porous media, *Water Resources Research*, 29(6), 1777–1785, doi:10.1029/93WR00385.
- Kang, P. K., M. Dentz, T. Le Borgne, and R. Juanes (2015), Anomalous transport on regular fracture networks: Impact of conductivity heterogeneity and mixing at fracture intersections, *Physical Review E*, 92(2), 1–15, doi:10.1103/PhysRevE.92.022148.
- Knackstedt, M. A., A. P. Sheppard, and M. Sahimi (2001), Pore network modelling of two-phase flow in porous rock : the effect of correlated heterogeneity, *Advances in water resources*, 24(3-4), 257–277.
- Lehmann, P., and D. Or (2009), Evaporation and capillary coupling across vertical textural contrasts in porous media, *Physical Review E*, 80(4), doi:10.1103/PhysRevE.80.046318.
- Lehmann, P., and D. Or (2013), Effect of wetness patchiness on evaporation dynamics from drying porous surfaces, *Water Resources Research*, 49(12), 8250–8262, doi:10.1002/2013WR013737.
- Lehmann, P., S. Assouline, and D. Or (2008), Characteristic lengths affecting evaporative drying of porous media, *Physical Review E*, 77(5), 1–16, doi:10.1103/PhysRevE.77.056309.

- Mani, V., and K. K. Mohanty (1999), Effect of pore-space spatial correlations on two-phase flow in porous media, *Journal of Petroleum Science and Engineering*, 23(3-4), 173–188, doi:10.1016/S0920-4105(99)00015-7.
- Metzger, T., and E. Tsotsas (2005), An influence of pore size distribution on drying kinetics : a simple capillary model, *Drying Technology*, 23(9-11), 1797–1809.
- Nachshon, U., N. Weisbrod, M. I. Dragila, and A. Grader (2011), Combined evaporation and salt precipitation in homogeneous and heterogeneous porous media, *Water Resources Research*, 47(3), 1–16, doi:10.1029/2010WR009677.
- Norouzi Rad, M., N. Shokri, and M. Sahimi (2013), Pore-scale dynamics of salt precipitation in drying porous media, *Physical Review E*, 88(3), 032,404, doi:10.1103/PhysRevE.88.032404.
- Or, D., P. Lehmann, E. Shahraeeni, and N. Shokri (2013), Advances in Soil Evaporation Physics A Review, *Vadose Zone Journal*, doi:10.2136/vzj2012.0163.
- Pillai, K., M. Prat, and M. Marcoux (2009), A study on slow evaporation of liquids in a dual-porosity porous medium using square network model, *International Journal of Heat and Mass Transfer*, 52(7-8), 1643–1656, doi:10.1016/j.ijheatmasstransfer.2008.10.007.
- Prat, M. (2011), Pore Network Models of Drying, Contact Angle, and Film Flows, 34(7), 1029–1038, doi:10.1002/ceat.201100056.
- Rajaram, H., L. a. Ferrand, and M. a. Celia (1997), Prediction of relative permeabilities for unconsolidated soils using pore-scale network models, *Water Resources Research*, 33(1), 43–52, doi:10.1029/96WR02841.
- Shahraeeni, E., P. Lehmann, and D. Or (2012), Coupling of evaporative fluxes from drying porous surfaces with air boundary layer: Characteristics of evaporation from discrete pores, *Water Resources Research*, 48(9), W09,525, doi:10.1029/2012WR011857.
- Shokri, N., P. Lehmann, and D. Or (2009), Characteristics of evaporation from partially wettable porous media, *Water Resour. Res.*, 45(2), W02,415, doi:10.1029/2008WR007185.
- Shokri, N., P. Lehmann, and D. Or (2010), Liquid-phase continuity and solute concentration dynamics during evaporation from porous media: Pore-scale processes near vaporization surface, *Physical Review E*, 81(4), 1–7, doi:10.1103/PhysRevE.81.046308.
- Toussaint, R., K. Måløy, Y. Méheust, G. Løvoll, M. Jankov, G. Schäfer, and J. Schmittbuhl (2012), Two-Phase Flow: Structure, Upscaling, and Consequences for Macroscopic Transport Properties, *Vadose Zone Journal*, 11(3), doi:10.2136/vzj2011.0123.
- Xu, L., S. Davies, A. B. Schofield, and D. A. Weitz (2008), Dynamics of drying in 3D porous media, *Phys. Rev. Lett.*, 101, 094,502, doi:10.1103/PhysRevLett.101.094502.